

Article

Water Pumping System Supplied by a PV Generator and with a Switched Reluctance Motor Using a Drive Based on a Multilevel Converter with Reduced Switches

Vitor Fernão Pires ^{1,2,3,*} , Daniel Foito ^{1,2,4} , Armando Cordeiro ^{2,4,5} , Tito G. Amaral ^{1,2}, Hao Chen ⁶, Armando Pires ^{1,2,3}  and João F. Martins ^{3,7} 

¹ ESTSetúbal, DEE, IPS—Instituto Politécnico de Setúbal, 2914-508 Setúbal, Portugal

² Sustain.RD, IPS—Instituto Politécnico de Setúbal, 2914-508 Setúbal, Portugal

³ INESC-ID Lisboa, 1000-029 Lisboa, Portugal

⁴ UNINOVA-CTS, UNL, 2829-516 Caparica, Portugal

⁵ Instituto Superior de Engenharia de Lisboa ISEL, DEEEA, IPL—Instituto Politécnico de Lisboa, 1549-020 Lisboa, Portugal

⁶ School of Electrical Engineering, China University of Mining and Technology, Xuzhou 221000, China

⁷ FCT, DEEC, UNL—Universidade Nova de Lisboa, 2829-516 Caparica, Portugal

* Correspondence: vitor.pires@estsetubal.ips.pt

Abstract: Pumping systems play a fundamental role in many applications. One of the applications in which these systems are very important is to pump water. However, in the real world context, the use of renewable energies to supply this kind of system becomes essential. Thus, this paper proposes a water pumping system powered by a photovoltaic (PV) generator. In addition, due to its interesting characteristics, such low manufacturing cost, free of rare-earth elements, simple design and robustness for pumping systems, a switched reluctance motor (SRM) is used. The power electronic system to be used in the PV generator and to control the SRM consists of a DC/DC converter with a bipolar output and a multilevel converter. The adopted DC/DC converter uses only one switch, so its topology can be considered as a derivation of the combination of a Zeta converter with a buck–boost converter. Another important aspect is that this converter allows continuous input current, which is desirable for PV panels. The topology selected to control the SRM is a multilevel converter. This proposed topology was adopted with the purpose of reducing the number of power semiconductors. A maximum power point algorithm (MPPT) associated with the DC/DC converter to obtain the maximum power of the PV panels is also proposed. This MPPT will be developed based on the concept of the time derivative of the power and voltage. It will be verified that with the increase in solar irradiance, the generated power will also increase. From this particular case study, it will be verified that changes in the irradiance from 1000 W/m² to 400 W/m² will correspond to a change in the motor speed from 1220 rpm to 170 rpm. The characteristics and operation of the proposed system will be verified through several simulation and experimental studies.

Keywords: renewable energy; photovoltaic generator (PV); switched reluctance motor (SRM); water pumping system; DC/DC converter; multilevel converter



Citation: Pires, V.F.; Foito, D.; Cordeiro, A.; Amaral, T.G.; Chen, H.; Pires, A.; Martins, J.F. Water Pumping System Supplied by a PV Generator and with a Switched Reluctance Motor Using a Drive Based on a Multilevel Converter with Reduced Switches. *Designs* **2023**, *7*, 39. <https://doi.org/10.3390/designs7020039>

Academic Editors: Loránd Szabó and Feng Chai

Received: 30 December 2022

Revised: 17 February 2023

Accepted: 28 February 2023

Published: 3 March 2023



Copyright: © 2023 by the authors. Licensee MDPI, Basel, Switzerland. This article is an open access article distributed under the terms and conditions of the Creative Commons Attribution (CC BY) license (<https://creativecommons.org/licenses/by/4.0/>).

1. Introduction

One of the applications in which electrical machines have been playing a very important role is related to water pumping. In fact, water pumps have been used for many purposes, such as agriculture, residences, industry and commerce. One aspect associated with these applications that has been considered, especially in recent years, is the supply of these water pumping systems from renewable energy sources. Some examples can be found in the following literature. The work proposed in [1] presents a review on solar, wind and hybrid wind–PV water pumping systems. Similarly, paper [2] also presents a review of solar-powered water pumping systems. The study presented in [3] demonstrated

a viability case study of solar/wind for water pumping systems in the Algerian Sahara regions. Research paper [4] proposes a solution for reducing carbon emissions by integrating urban water systems and solar-powered systems. One of the renewable energy sources that have been considered to be highly applicable is photovoltaic generators. In rural and remote areas, this kind of renewable energy source has even been considered to be extremely important. For example, in [5], a photovoltaic water pumping system for horticultural crop irrigation in Mozambique is proposed. A comprehensive review on solar-powered water pumping systems for irrigation developments and prospects towards green energy is presented in [6]. A case study regarding the feasibility of renewable energy sources for pumping clean water in sub-Saharan Africa is described in [7]. In [8], a PV microgrid design for rural electrification that can be applied to water pumping systems and other systems is proposed. There are several factors that must be considered in the design and application of these systems, such as, for example, the cost and reliability. Thus, besides the PV panels, in the design and choice of these systems, the power electronics and machine characteristics must be considered.

Several electrical machine types have been used for water pumping systems. Among them, one that has been recently used is the switched reluctance machine (SRM). This machine has been adopted due to several important characteristics, such as low manufacturing cost, free of rare-earth elements, simple design, robustness and efficiency. For example, in [9], a design and optimization model of a high-speed switched reluctance motor is proposed. A comparison of design and performance parameters in switched reluctance and induction motors is presented in [10], showing the main important characteristics of the SRM. It should be mentioned that some of the characteristics, such as low cost and reliability, are very interesting in pumping systems, especially for developing countries. Some examples of the importance of pumping systems in developing countries can be found in [11] applied to certain regions of India, or Latin American countries [12]. Another aspect of these pumping systems is the required power electronic converters to operate the SRM. Several types of power converter topologies have been proposed for this machine. One group of topologies that has been used is characterized by the application of two voltage levels to the motor windings. Some examples of two-voltage-level topologies can be found in [13]. A review of switched reluctance motor converter topologies, including two voltage levels, can also be found in [14]. Another group that is now becoming very popular is characterized by applying more than two levels to the motor winding. These topologies, designated as multilevel, present several advantages, such as reduced switching frequency, reduced current ripple, lower voltage rate of power semiconductor devices, faster motor phase magnetization and demagnetization and inherent fault-tolerant capability. For example, the review proposed in [15] summarizes several SRM multilevel topologies. A performance comparison of multilevel converter topologies for high-power high-speed switched reluctance machines can be found in [16]. A torque ripple analysis of several multilevel converter topologies for switched reluctance machines can be found in [17]. As well as the two-level converters, the majority of these multilevel structures present an asymmetric configuration. The first topologies were derived from the classical multilevel converters used, for example, for induction motors. In this way, the flying capacitor (AFC), asymmetric neutral point clamped (ANPC) and cascaded H-bridge were usually proposed, as described in the next references. An asymmetric three-level neutral point diode clamped converter topology for SRM drives is proposed in [18]. Another asymmetric neutral point diode clamped topology considering reduced component count for SRM drives can be found in [19]. An asymmetric flying capacitor multilevel H-bridge inverter for SRM drives can be found in [20]. A cascade multilevel converter of SRM drives is proposed in [21]. It is also possible to find several of these topologies in [22], now considering torque ripple minimization with multicarrier PWM strategies. This application also has been extended to other kinds of multilevel topologies. One of them is the *T-Type*, although the required blocking voltage of power devices is not the same. An asymmetric three-level T-Type converter for SRM drives applied to hybrid electric vehicles is presented in [23].

Additionally, an advanced multi-level converter for four-phase SRM drives based on the *T-Type* converter can be found in [24]. Another solution is the modular multilevel converter (MMC). However, since this topology consists of a higher number of power converters, it has been used for applications in which a decentralized battery energy storage system is required [25] or hybrid electric vehicle applications [26]. Meanwhile, many other topologies have been proposed. Some of them take into consideration specific applications, for example, electric vehicles or pumping systems. A comparative review of SRM converters for electric vehicle applications can be found in [27]. A multi-battery block module power converter for electric vehicles driven by a switched reluctance motors is proposed in [28]. A multi-purpose fault-tolerant multilevel topology for an 8/6 SRM drive is proposed in [29]. A novel converter topology for a photovoltaic water pump based on switched reluctance motors can be found in [30]. Additionally, a grid-interfaced solar PV water pumping system with energy storage is proposed in [31]. Others take into consideration specific factors, such as fast magnetizing and demagnetizing [32] or fault tolerance of the power semiconductors of the converter [33]. However, one important disadvantage is related to the higher number of power semiconductors.

In addition to the drive associated with the machine, a DC/DC converter associated with the PV panels must also be considered in these pumping systems. These DC/DC converters are also associated with MPPT (maximum power point) algorithms to constantly maintain the PV panels at full power. There are many DC/DC power converter topologies that have been proposed for this kind of system. Usually, these DC/DC converters are designed for a single output. Some examples where a single output is required can be found in following examples. In [34], a simplified PWM MPPT approach for a direct PV-fed switched reluctance motor in a water pumping system using a DC/DC converter is proposed. Other renewable energy-fed switched reluctance motors for PV pump applications requiring a DC/DC converter with single output can be found in [35]. A PI controller design for the MPPT of a photovoltaic system supplying SRM via the *BAT-inspired* search algorithm is presented in [36]. A similar solution of MPPT control design of a PV system supplying SRM considering the *BAT-inspired* search algorithm is proposed in [37]. An analysis and study regarding the performance of several DC/DC converters that are indicated to be used in BLDC motor drive applications is presented in [38]. However, several solutions have been proposed in which a dual output is required for the SRM drive DC/DC converters. Some examples of these type of converters can be found in the next references. A sensorless SRM-driven solar irrigation pump with grid support using the Vienna rectifier requiring dual output voltages is presented in [39]. A three-level quadratic boost DC/DC converter associated with an SRM drive for photovoltaic water pumping requiring dual output voltages is proposed in [40]. Another topology presenting dual output voltages for a four-phase SRM-driven solar-powered water pumping solution can be found in [41]. These solutions present boost characteristic and require two switches. Thus, in [42], another boost converter with a dual output but with only one switch is presented. DC/DC converters characterized by *buck-boost* operation were also proposed to be used for this kind of. In [43], a DC/DC buck-boost converter for a PV pumping system that uses an SRM is proposed. A similar approach was also used by [44]. However, in this case, a new configuration of a dual-output buck-boost converter was used. In [45], a DC/DC converter with dual output but based on *Luo* converters and with an advanced voltage-lift technique is proposed. A topology with similar characteristics is also proposed by [46], but in this case, a topology based on a combination of the *SEPIC* and *Cuk* converters was used. It should be noted that, in the case of motor drives with multilevel topologies, it is usual to supply them with two or more outputs. Some solutions using multilevel topologies for other types of motors can also be found in the literature. A boost multilevel NPC-fed asynchronous pumped storage hydro-generating unit is proposed in [47]. An isolated cascaded multilevel *qZSI* converter for a single-phase induction motor for water pump application can be found in [48]. A PV generator-fed water pumping system based on an SRM with a multilevel fault-tolerant converter is proposed in [49]. An NPC inverter-based solar PV-fed induction motor drive

for water pumping is proposed in [50]. However, one aspect of these solutions is that the design of the drive is not usually optimized taking into consideration the reduction in the power semiconductor switches and/or passive components. On the other hand, most solutions have not considered water pumping systems based on SRM drives connected to multilevel converters. Another aspect associated with these PV pumping systems is the MPPT algorithm that must be associated with the power electronic converters. Many different approaches have been proposed for the implementation of these algorithms. Among them, the algorithms that are most used and also considered as classical ones are the perturb and observe and the incremental conductance [51]. Other algorithms that use metaheuristic optimization techniques have also been proposed. Examples of these can be seen in works [52,53]. Although these algorithms usually allow excellent results to be obtained, their implementation usually requires some complexity.

Taking into consideration the aspects already mentioned, this paper proposes a PV-powered water pumping system in which an SRM is used. In this proposal, the SRM drive is composed of a multilevel converter with a reduced number of power devices [54]. On the other hand, a combined DC/DC converter associated with the PV panels is also proposed, which was designed with a single switch [55]. This DC/DC converter presents a buck–boost characteristic and continuous input current. Associated with this DC/DC converter, the use of an MPPT algorithm based on the concept of the time derivative of the power and voltage is also proposed. It should be mentioned that the adoption of this algorithm was chosen taking into consideration its simplicity and possibility to be implemented with a simple analogue electric circuit. Finally, the proposed system for the PV-powered water pumping system will be tested in two ways. Firstly, through a computer simulation, and secondly, using a laboratory prototype.

Regarding the organization of this paper, it consists of six sections, the first one being this introduction. In the next section, the proposed water pumping system supplied by PV panels and with an SRM drive based on a multilevel converter with reduced switches will be presented. The control system developed for this application will be presented in the third section. In the fourth section, several results that were obtained through a simulation program will be presented. These results will also be confirmed using a laboratory prototype, with the obtained results presented in Section 5. Section 6 is dedicated to the discussion of the results and comparison with other solutions. Finally, in the last section, the conclusions of this work will be presented.

2. Proposed Water Pumping System Supplied by a PV Generator

The proposed water pumping system will be driven by an 8/6 SRM. In addition, it will be fed by a renewable energy source, namely by PV panels. To obtain the maximum power from the PV generators, a DC/DC converter with dual output is proposed. To obtain the dual output, a converter derived from a combination of the Zeta converter with a buck–boost converter is used. This combination allows a single switch to be used. Another aspect is that the input current of the converter (output PV current) will be continuous. The SRM drive is composed of a multilevel converter that will be supplied by the dual output of the DC/DC converter. The proposed water pumping system is presented in Figure 1.

As described and presented in Figure 1, the electronics associated with the pumping system consist of two converters. These converters can be analyzed in a separated way as described in the next section.

In the context of this paper, the water pump is a mechanical device where the shaft is coupled to the SRM using an appropriate transmission. The use of a centrifugal water pump is assumed, since this is one of the most common types of pumps for transferring fluids. The centrifugal pump operates on a concept called forced vortex flow. This means that when a specific quantity of fluid is forced to rotate imposed by an external torque,

there is a rise in the rotating liquid’s pressure head, which transfers the fluid from one place to another. The necessary external torque to move the impeller is given by:

$$T_{ext} = \frac{\rho g H_T Q}{\omega \eta} \tag{1}$$

where ρ is the water density in (kg/m^3), g is the acceleration due to gravity (m/s^2), H_T is the pump’s total head (m), Q is the water flow rate (m^3), ω is the speed of the impeller (rad/s) and η is the efficiency of the pump. The operation limits of this application for water pumping purposes should be determined by the minimum water flow rate required and necessary head (elevation) according to pump characteristic (typical operation curve) such as speed and efficiency.

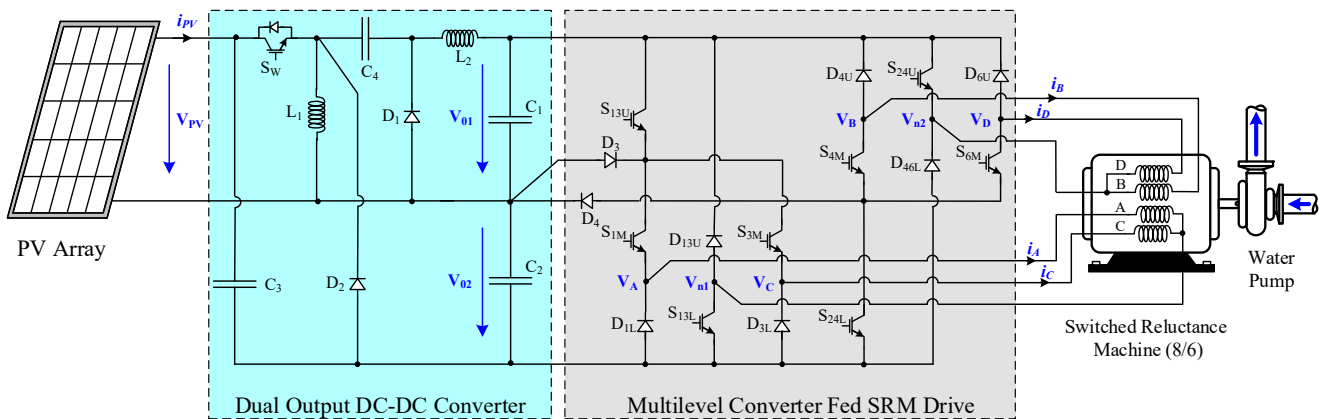


Figure 1. Water pumping system supplied by a PV generator and with an SRM using a drive based on a multilevel converter with reduced switches.

2.1. Multilevel Converter Fed SRM Drive

The proposed multilevel converter adopted in the SRM drive was designed with the purpose of minimizing the number of components. In this way, although allowing the application of multilevel voltages to the 8/6 SRM, it only requires eight transistors and eight diodes. Analyzing the possible combinations for the transistor state (ON/OFF) conditions, it is possible to conclude that there are five working modes associated with each motor winding, respectively (example given for motor winding A):

Mode 1: This mode is verified when the devices S_{13U} , S_{1M} and S_{13L} are in the ON condition. As shown in Figure 2a, this circuit applies the two input DC voltages ($V_{C1} = V_{o1}$ and $V_{C2} = V_{o2}$) to the motor winding. In this mode, the maximum positive voltage applied to the motor winding is $(+V_{C1} + V_{C2})$.

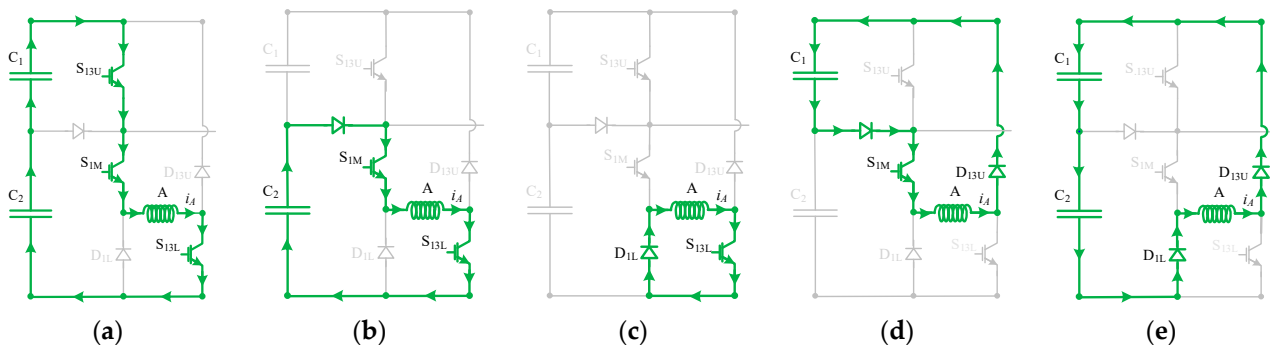


Figure 2. Operating modes associated with each motor winding: (a) Mode 1 $\rightarrow +V_{C1} + V_{C2}$, (b) Mode 2 $\rightarrow +V_{C2}$, (c) Mode 3 $\rightarrow 0$, (d) Mode 4 $\rightarrow -V_{C1}$, (e) Mode 5 $\rightarrow -V_{C1} - V_{C2}$.

Mode 2: In this mode, the transistors S_{1M} and S_{13L} are in the *ON* condition, and the resulting circuit allows the application of the intermediate positive voltage ($+V_{C2}$) to the motor winding. Figure 2b presents the diagram of this circuit.

Mode 3: In this mode, the converter applies the zero-voltage level to the motor winding. This circuit is obtained when only S_{13L} is in the *ON* condition (see Figure 2c).

Mode 4: In this mode, the circuit allows the application of the intermediate negative voltage level ($-V_{C1}$) to the motor winding. This circuit results from the condition in which only the transistor S_{1M} is in the *ON* condition (see Figure 2d).

Mode 5: This mode is verified when none of the transistors are in the *ON* condition. As shown in Figure 2e, the circuit applies the maximum reverse voltages of the two input DC sources (V_{C1} and V_{C2}) to the motor winding. Therefore, the maximum negative voltage applied to the winding is ($-V_{C1} - V_{C2}$).

These operating modes can also be presented mathematically. Thus, for the development of the mathematical model, the power semiconductors are considered as ideal switches. In this way, associated with the transistors, Boolean variables are considered, as described by (2):

$$\begin{cases} \alpha_{ji} = 0 \text{ if } S_{ji} \text{ is ON} \\ \alpha_{ji} = 0 \text{ if } S_{ji} \text{ is OFF} \\ \alpha_{km} = 0 \text{ if } S_{km} \text{ is ON} \\ \alpha_{km} = 0 \text{ if } S_{km} \text{ is OFF} \end{cases} \quad (2)$$

where $k = 1, 3, 4, 6, j = 13, 24$ and $I = U, M$.

Using these variables, taking into consideration the possible combinations for the transistors' *ON/OFF* conditions and in accordance with the Kirchhoff laws, it is possible to obtain the mathematical expressions of the voltages applied to the motor windings, as function of the switches. These expressions are then given by:

$$\begin{bmatrix} V_{An1} \\ V_{Bn2} \\ V_{Cn1} \\ V_{Dn2} \end{bmatrix} = \begin{bmatrix} \alpha_{13U}\alpha_{1M}\alpha_{13L} - \beta_A & \alpha_{1M}\alpha_{13L} - \beta_A \\ \alpha_{4M}\alpha_{24U} - \beta_B & \alpha_{24L}\alpha_{4M}\alpha_{24U} - \beta_B \\ \alpha_{13U}\alpha_{3M}\alpha_{13L} - \beta_C & \alpha_{3M}\alpha_{13L} - \beta_C \\ \alpha_{6M}\alpha_{24U} - \beta_B & \alpha_{24L}\alpha_{6M}\alpha_{24U} - \beta_B \end{bmatrix} \begin{bmatrix} V_{o1} \\ V_{o2} \end{bmatrix} \quad (3)$$

where β is binary variable that is a function of:

$$\begin{cases} \beta_w = 1 \text{ if } i_w > 0 \text{ and all } S \text{ associated to winding } w \text{ are OFF} \\ \beta_w = 0 \text{ if } i_w \leq 0 \text{ or all } S \text{ associated to winding } w \text{ are not OFF} \end{cases} \quad (4)$$

where $w = A, B, C, D$.

According to the previous expressions, it is possible to confirm the multilevel voltage operation of the converter, namely by verifying that five different voltage levels can be applied.

2.2. Operation in Continuous Conduction Mode

Similar to the SRM drive that operates the motor, the DC/DC converter was also designed with a reduced component count. In this way, although the converter has the specification of having two outputs, it only requires one switch. Thus, considering that the converter operates in continuous conduction mode (CCM), it is possible to conclude that there are only two working modes, respectively:

Mode 1: This mode is verified when the converter switch S_w is in the *ON* state and diodes D_1 and D_2 are in the *OFF* state, resulting in the circuit configuration of Figure 3a. In this mode, both inductors (L_1 and L_2) are in charging mode, through which their currents will increase. Inductor L_1 will be charged by the input power source. On the other hand, the capacitors C_3 and C_4 will discharge their storage energy to the inductor L_2 and to the load. In this mode, capacitors C_1 and C_2 will also discharge to the load. The equations for

the inductors' voltages and capacitors' currents in this mode are as follows, where i_{load} is the nominal current of the SRM:

$$\begin{cases} v_{L1} = L_1 \frac{di_{L1}}{dt} = V_{PV} = V_i \\ v_{L2} = L_2 \frac{di_{L2}}{dt} = V_i + V_{C4} - V_{C1} \\ i_{C3} = C_2 \frac{dv_{C3}}{dt} = i_{load} + i_{C2} \\ i_{C4} = C_4 \frac{dv_{C4}}{dt} = -i_{L2} \end{cases} \quad (5)$$

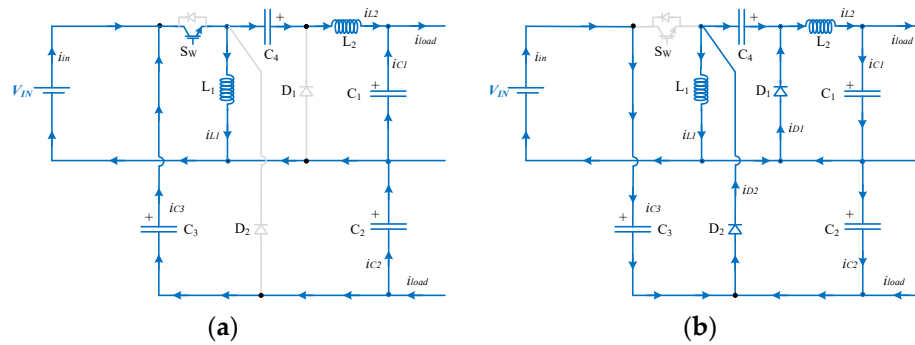


Figure 3. Operating modes of the DC/DC converter: (a) Mode 1: $S_W \rightarrow ON$, (b) Mode 2: $S_W \rightarrow OFF$.

Mode 2: In this mode, the converter switch S_w changes to the OFF state. In an opposite way, diodes D_1 and D_2 change to the ON state, resulting in the circuit presented in Figure 3b. In contrast to mode 1, in this mode, both inductors (L_1 and L_2) will be in discharging mode. In this way, their current will decrease. The capacitors C_3 and C_4 will be in charging mode, through which inductor L_1 will discharge to such capacitors. Inductor L_2 will discharge to capacitors C_1 and C_2 . The equations for the inductors' voltages and capacitors' currents in this mode are as follows:

$$\begin{cases} v_{L1} = L_1 \frac{di_{L1}}{dt} = V_i - V_{C3} = -V_{C4} \\ v_{L2} = L_2 \frac{di_{L2}}{dt} = -V_{C1} \\ i_{C3} = C_2 \frac{dv_{C3}}{dt} = \frac{i_{L1}}{2} \\ i_{C4} = C_4 \frac{dv_{C4}}{dt} = \frac{i_{L1}}{2} \end{cases} \quad (6)$$

One aspect that is possible to verify from these modes is that the PV current (input of the converter) will be continuous. The converter waveforms associated with the two operating modes are presented in Figure 4.

Taking into consideration both operating modes and the zero average voltage in both inductors over one cycle, the static voltage gain of this DC/DC converter can be obtained. The average voltages in the inductors are given by:

$$\begin{cases} \frac{1}{T} \int_0^T v_{L1} dt = \frac{1}{T} \left[\int_0^{\delta T} (V_i) dt + \int_{\delta T}^T (-V_{C4}) dt \right] = 0 \\ \frac{1}{T} \int_0^T v_{L1} dt = \frac{1}{T} \left[\int_0^{\delta T} (V_i) dt + \int_{\delta T}^T (V_i - V_{C3}) dt \right] = 0 \\ \frac{1}{T} \int_0^T v_{L2} dt = \frac{1}{T} \left[\int_0^{\delta T} (V_i + V_{C4} - V_{C1}) dt + \int_{\delta T}^T (-V_{C1}) dt \right] = 0 \end{cases} \quad (7)$$

Taking into account the expressions given by (5) and (6), the converter static voltage gain of each output and capacitor voltages can be obtained, which are given by:

$$\begin{cases} V_{o1} = V_{C1} = \frac{\delta}{1-\delta} V_i \\ V_{o2} = V_{C2} = \frac{\delta}{1-\delta} V_i \\ V_o = V_{C1} + V_{C2} = \frac{2\delta}{1-\delta} V_i \\ V_{C3} = \frac{1}{1-\delta} V_i \\ V_{C4} = \frac{\delta}{1-\delta} V_i \end{cases} \quad (8)$$

From the expressions given in (8), it is possible to see that the static voltage gains of both outputs are equal and have a *buck–boost* characteristic.

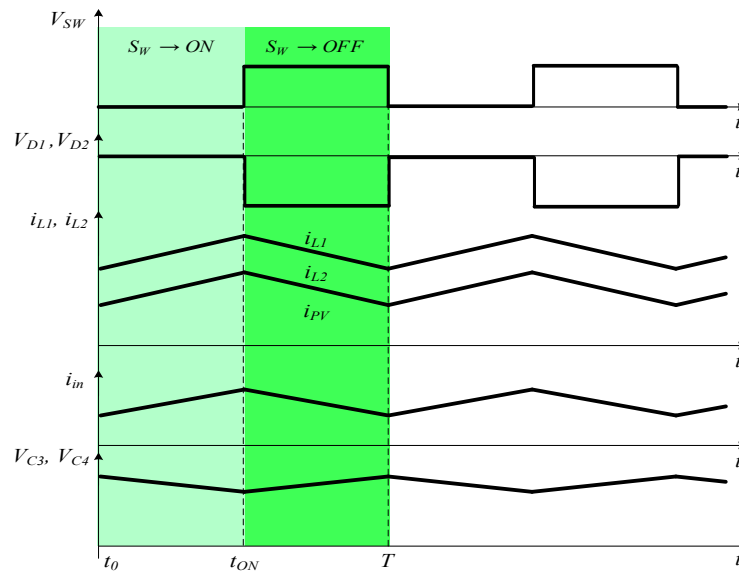


Figure 4. Waveforms associated with both operating modes.

2.3. DC/DC Component Design

This section presents the design of the components of the *DC/DC buck–boost* converter. During mode 1, the capacitor C_4 discharges according to the i_{L2} current (see Figure 3a) given by Equation (9).

$$\Delta V_{C4} = \frac{1}{C_4} \int_0^{\delta T} i_{L2} dt \quad (9)$$

Therefore, is possible to design the capacitor for a permissible voltage ripple. The previous equation can also be expressed as (10), where δ is the duty cycle and f_{sw} the switching frequency.

$$C_4 = \frac{i_{L2} \cdot \delta}{\Delta V_{C4} \cdot f_{sw}} \quad (10)$$

Considering that the average current over the output capacitor C_1 in each cycle is zero, the capacitor C_4 value depends on the load current, resulting in Equation (11).

$$C_4 = \frac{i_{load} \cdot \delta}{\Delta V_{C4} \cdot f_{sw}} \quad (11)$$

Inserting the duty cycle and considering Equation (8), this leads to Equation (12).

$$C_4 = \frac{i_{load}}{\Delta V_{C4} \cdot f_{sw}} \cdot \frac{V_{C1}}{(V_i + V_{C1})} = \frac{i_{load}}{\Delta V_{C4} \cdot f_{sw}} \cdot \frac{V_o}{(2V_i + V_o)} = \frac{P_{out}}{(2V_i + V_o) \cdot \Delta V_{C4} \cdot f_{sw}} \quad (12)$$

From the charge variation of C_3 , it is possible to conclude that the voltage across C_3 decreases during mode 1, which leads to:

$$\Delta V_{C3} = \frac{1}{C_1} \int_0^{\delta T} i_{C3} dt \quad (13)$$

Similarly, one can also design the capacitor C_3 for a permissible voltage ripple as happens with capacitor C_4 , Equation (14).

$$C_3 = \frac{i_{C3} \cdot \delta}{\Delta V_{C3} \cdot f_{sw}} \quad (14)$$

Considering that the average current over the output capacitor C_3 in each cycle is zero, the capacitor C_3 value depends on the load current, resulting in Equation (15):

$$C_3 = \frac{i_{load} \cdot \delta}{\Delta V_{C3} \cdot f_{sw}} \quad (15)$$

Inserting the duty cycle and considering Equation (8), this now leads to Equation (16).

$$C_3 = \frac{i_{load}}{\Delta V_{C3} \cdot f_{sw}} \cdot \frac{V_{C2}}{(V_i + V_{o2})} = \frac{i_{load}}{\Delta V_{C3} \cdot f_{sw}} \cdot \frac{V_o}{(2V_i + V_o)} = \frac{P_{out}}{(2V_i + V_o) \cdot \Delta V_{C3} \cdot f_{sw}} \quad (16)$$

In general, the differential Equation (17) represents the current evolution on a capacitor C_2 .

$$i_{C2}(t) = C_2 \frac{dv_{C2}(t)}{dt} \quad (17)$$

After linearization, Equation (17) becomes Equation (18).

$$\frac{\Delta v_{C2}}{\Delta t} = \frac{i_{C2}}{C_2} \quad (18)$$

During mode 1, the instantaneous current in the capacitor C_2 is equal to the output current. Additionally, in mode 1, we have $\Delta t = \delta T_{sw} = \delta / f_{sw}$, thus:

$$C_2 = \frac{i_{load} \cdot \delta}{\Delta V_{C2} \cdot f_{sw}} = \frac{i_{load}}{\Delta V_{C2} \cdot f_{sw}} \cdot \frac{V_o}{(2V_i + V_o)} = \frac{P_{out}}{(2V_i + V_o) \cdot \Delta V_{C1} \cdot f_{sw}} \quad (19)$$

Observing Figure 4, it is possible to verify that when the power semiconductor is turned on, the charge variation ΔQ over the capacitor C_1 is equivalent to the area of a triangle with $0.5\Delta I_{L2}$ height and time base $0.5T_{sw}$, thus:

$$C_1 = \frac{\Delta Q}{\Delta V_{C1}} = \frac{\frac{1}{2f_{sw}} \cdot \frac{\Delta I_{L2}}{2}}{\Delta V_{C1}} = \frac{\Delta I_{L2}}{8\Delta V_{C1}f_{sw}} \quad (20)$$

Similar calculations can be performed to obtain the values of both inductors. During mode 1, the input voltage lies across L_1 and the current through it increases by ΔI_{L1} . The inductor L_1 can be obtained for a chosen current ripple according to Equation (21).

$$L_1 = \frac{V_i \cdot \delta}{\Delta I_{L1} \cdot f_{sw}} \quad (21)$$

Replacing the duty cycle given in (8), it is possible to obtain Equation (22).

$$L_1 = \frac{V_i}{\Delta I_{L1} \cdot f_{sw}} \cdot \frac{V_o}{(2V_i + V_o)} \quad (22)$$

During mode 1, the voltage across L_2 is given by Equation (5), and the current through it increases by ΔI_{L2} . The inductor L_2 can be obtained for a chosen current ripple according to (23).

$$L_2 = \frac{(V_i + V_{C4} - V_{C1}) \cdot \delta}{\Delta I_{L2} \cdot f_{SW}} \tag{23}$$

Replacing the duty cycle and other relations given in Equation (8), it is possible to obtain (24).

$$L_2 = \frac{(V_i + V_{C4} - V_{C1})}{\Delta I_{L2} \cdot f_{SW}} \cdot \frac{V_0}{(2V_i + V_0)} \tag{24}$$

The maximum reverse voltage of the converter switch S_w and maximum continuous current are given by Equations (25) and (26).

$$V_{R-SW} = V_i - V_{L1} = V_i + V_{C4} \tag{25}$$

$$I_{C-SW} = i_{L1} \tag{26}$$

When the converter switch S_w is turned on, diodes D_1 and D_2 are turned off. In this situation, the maximum reverse voltage and maximum continuous current over D_1 (during the ON state) are given by (27) and (28), respectively.

$$V_{R-D1} = V_{C4} - V_i \tag{27}$$

$$I_{C-D1} = i_{L1} - i_{C3} = \frac{i_{L1}}{2} \tag{28}$$

Similarly, for the diode D_2 , we have Equations (29) and (30).

$$V_{R-D2} = V_{C3} \tag{29}$$

$$I_{C-D2} = i_{C2} + i_{C3} + I_{load} \tag{30}$$

To analyze the design of these components, an example of the determination of their values is now presented. The following calculations are based on Equations (8)–(30) to estimate the component values. A DC voltage of 40 V and a DC output voltage of 200 V are assumed, which results in a duty cycle of:

$$\delta = \frac{V_0}{(2V_i + V_0)} = 0.71 \tag{31}$$

Considering a switching frequency $f_{sw} = 10$ kHz and assuming a maximum variation of 0.5 A in L_1 (ΔI_{L1}), it is possible to calculate the value of inductor L_1 based on Equation (21):

$$L_1 = \frac{40 \times 0.71}{0.5 \times 10^4} \approx 5.6 \text{ mH} \tag{32}$$

Considering the duty cycle of Equation (30), the input voltage $V_i = 40$ V and the voltages of capacitors C_1 and C_4 given by Equation (8), and assuming a maximum variation of 0.5 A in L_2 (ΔI_{L2}), it is possible to calculate the value of inductor L_2 based on Equation (23):

$$L_2 = \frac{(40 + 138 - 100) \times 0.71}{0.5 \times 10^4} \approx 11.2 \text{ mH} \approx 2L_1 \tag{33}$$

Assuming an output power of 1500 W and considering that C_3 and C_4 achieve a voltage variation of 2%, is possible to calculate the values of these capacitors according Equations (12) and (16):

$$C_3 = C_4 = \frac{1500}{(2 \times 40 + 200) \times 0.02 \times 138 \times 10^4} \approx 194 \text{ } \mu\text{F} \tag{34}$$

In the same conditions, assuming that the output capacitors C_1 and C_2 achieve a voltage variation of 1%, is possible to calculate the values of these capacitors according Equations (19) and (20):

$$C_1 = \frac{0.5}{8 \times 0.01 \times 100 \times 10^4} \approx 6.25 \mu\text{F} \tag{35}$$

$$C_2 = \frac{1500}{(2 \times 40 + 200) \times 0.01 \times 100 \times 10^4} \approx 535 \mu\text{F} \tag{36}$$

3. Control of the Proposed System

Another aspect that must be taken into consideration is the control of the proposed pumping system. There are several aspects that should be considered, such as the extraction of the energy from the PV panels and the control of the motor. The control of the extracted energy from the PV panels will be ensured by the DC/DC converter. Thus, since the purpose is to extract the maximum energy, an MPPT algorithm will be considered. This algorithm will establish the control of the DC/DC converter switch. In order to maintain the balance between the generated energy from the PV panels and the motor consumption, there is a voltage controller associated with the motor drive. In this way, this voltage controller will ensure that the DC/DC converter output voltages will be stable at a specific reference value. A block diagram of the control system for the proposed solution is presented in Figure 5.

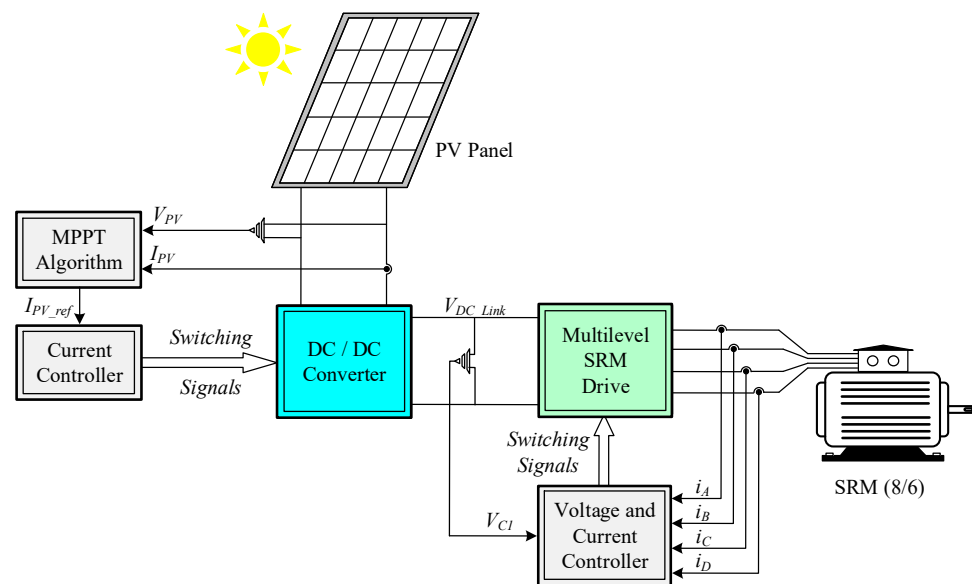


Figure 5. Control system for the proposed solution.

Regarding the MPPT algorithm that will ensure the harnessing of the maximum energy that the solar panels can supply, different approaches have been proposed. Among them, the algorithms that are most used are the incremental conductance and perturb and observe [51]. Other algorithms including the use of metaheuristic optimization techniques were proposed. Examples of these can be seen in works [52,53]. Although these algorithms usually allow excellent results to be obtained, their implementation usually requires some complexity. Thus, for this system, an approach considering its simplicity and possibility of being implemented with a simple analogue electric circuit will be used. This algorithm is based on the time derivative of power, as well as voltage. In this way, singularities are avoided that can be found with an algorithm based on the derivative of the power and voltage or current [56]. This algorithm will then be developed taking into consideration the typical $I-V$ curve of the PV panels. In accordance with this, the MPP is achieved when the derivative of the voltage and power are zero. However, the movement to that point can be

achieved through the derivative of the power and voltage in order of time. Therefore, if the system is within the left side of the *MPP* and if the condition $dP/dt > 0$ and $dV/dt > 0$ is ensured, this will result in a trajectory in the direction of the *MPP*. On the other hand, if the system is within the right side of the *MPP* and if the condition $dP/dt > 0$ and $dV/dt < 0$ is ensured, this will also result in a trajectory in the direction of the *MPP*. Thus, the conditions to ensure that the system will move to the *MPP* are given by (37).

$$\left\{ \begin{array}{l} \left(\frac{dP}{dt} > 0 \text{ and } \frac{dV}{dt} > 0 \right) \text{ or } \left(\frac{dP}{dt} < 0 \text{ and } \frac{dV}{dt} < 0 \right), \text{ decrease } I_{PH} \\ \left(\frac{dP}{dt} > 0 \text{ and } \frac{dV}{dt} < 0 \right) \text{ or } \left(\frac{dP}{dt} < 0 \text{ and } \frac{dV}{dt} > 0 \right), \text{ increase } I_{PH} \end{array} \right. \quad (37)$$

Starting from the conditions given by (37), the *MPPT* function regarding the derivative of voltage and power in order of time can be developed. Therefore, taking into consideration that the input current of the *DC/DC* converter is regulated by a hysteretic current controller, the reference current is given by the following control law:

$$i_{PV_ref} = k \int \frac{dP}{dt} \frac{dV}{dt} dt \quad (38)$$

However, it is possible to simplify the previous control law even more. To do so, instead of using the derivative of the power and voltage in order of time, their signal will simply be considered. In this way, the *MPPT* only consists of a single expression given by Equation (39), which can easily be implemented through an analogue electronic circuit.

$$i_{PV_ref} = k \int \text{sign}\left(\frac{dP}{dt}\right) \text{sign}\left(\frac{dV}{dt}\right) dt \quad (39)$$

One important aspect that must also be considered is the balance between the generated power and the power consumption of the motor. This will be ensured by the adopted voltage controller of the *SRM* drive. Therefore, this voltage controller must ensure that the output voltage of the proposed *DC/DC* converter remains in steady state in the reference value. To ensure this, the voltage controller will define the current references for the *SRM* drive controller. A *PI* compensator will be used for this voltage controller, as shown in Figure 6. Regarding the *PI* parameters, they have been determined through trial and error obtained from several repeated experiments.

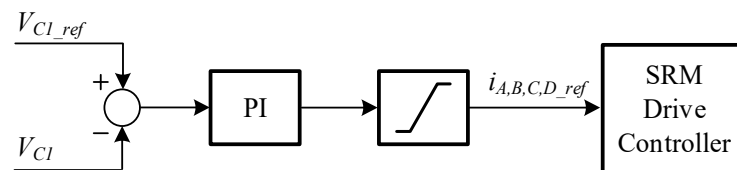


Figure 6. Voltage controller associated with the *SRM* drive.

4. Simulation Results

With the purpose of confirming the expected performance of the proposed solution, the system was initially implemented in a simulation software. The adopted program was one of the most used in these kinds of systems, namely the *Matlab/Simulink*. For the power electronic converters, inductors (L_1 and L_2) of 5 mH and 10 mH, respectively, and capacitors of 22 μ F (C_1), 680 μ F (C_2) and 220 μ F (C_3 and C_4) were used. It should be mentioned that these values are based on the previous determination of these components. However, they are not completely equal, since for the experimental tests, components that exist in the laboratory were used, and the same values that were used in that part were used for comparison purposes. Regarding the machine, an 8/6 *SRM* was used. Regarding the *PV* panels used in this system, their characteristics can be seen in Table 1. The component values of the power electronic converters were obtained from the equations presented in Section 2.3, and input *DC* voltage 40 V, *DC* output voltage 200 V, 1500 W output power,

$f_{sw} = 10$ kHz, a ripple limit in capacitor voltages $\Delta V_{C1} = \Delta V_{C2} \leq 1\%$, $\Delta V_{C3} = \Delta V_{C4} \leq 2\%$, and inductor current ripples $\Delta I_{L1} = \Delta I_{L2} < 10\%$ were used, which are values that are usually used by designers. However, the adopted values are higher since they have been chosen because of the existing components in our laboratory.

Several simulation tests are presented in this section. The first test was conducted with 700 W/m^2 (irradiance) and $25 \text{ }^\circ\text{C}$ (ambient temperature). The obtained waveforms of this test are presented in Figure 7. The waveforms of this figure are related to the voltage applied to winding A, with currents in all windings and input DC voltages applied to the drive (or DC/DC output voltages). From the analysis of the voltage applied to the motor winding A (Figure 7a), the multilevel operation of the drive is noticeable, where the two positive voltage levels are clearly visible. Moreover, it is possible to see that, initially, when the winding is magnetized and at the end when it is demagnetized, the maximum voltage levels are applied. One of the voltage levels that does not appear in this waveform is the $-V_{C1}$ (Figure 2d). The reason for this is because when the demagnetization is necessary, it should be carried out as fast as possible. In this way, the negative voltage that is applied is $-V_{C1} - V_{C2}$ (Figure 2e). Since there are no negative currents in this motor, there is no need to apply the negative voltage level $-V_{C1}$ (Figure 2d) to maintain a specific negative current level. On the other hand, the currents in the motor windings are clearly controlled, as visible from the waveforms presented in Figure 7b. Another aspect that can be seen is the effect of the switching action of the inverter devices on the SRM pulsation torque. As can be seen from Figure 7c, there are two different impacts. The first one is related to the high-frequency switching of the inverter devices originating from the hysteretic comparator. Since this hysteresis is low, the current ripple is also low, so the impact on the torque is also low. On the other hand, this high-frequency switching will affect the voltage applied to the motor windings but has a lower impact on the current. Due to this high frequency, the motor winding will behave as a low-pass filter. As a result, this will also attenuate the impact on the torque. However, the major problem appears during the transitions between the phase current, from which a pulsation torque will originate. This last problem can be attenuated using advanced control techniques. However, for this specific application, this is not significant. Finally, analyzing the waveforms of the input DC voltages applied to the drive (output voltages of the DC/DC converter) presented in Figure 7d, it is possible to see that they are balanced and stable at the reference value (set to 200 V). On the other hand, as shown in Figure 7e, the converter input current is continuous, which is one advantage considering the characteristics of the PV panels.

Table 1. Characteristics of the PV panels used in the proposed pumping system (in STC).

Parameter	Value
Voltage at MPP	37.4 V
Current at MPP	8.56 A
Power at MPP	320 W
Open-circuit voltage	46.7 V
Short-circuit current	9.10 A

Simulation tests in transient conditions were also carried out. In this condition, the system was suddenly connected considering the same values of the previous test, which can be seen in Figure 8 (notice that the voltages and currents of the capacitors and inductors are initially zero). Analyzing the output DC/DC converter voltage waveforms presented in Figure 8a, it is possible to see they started at 0 V and stabilized at 200 V (reference value) in a balanced state. It should be mentioned that until the output voltages reach the reference value, the pumping system is not operating. In this way, these results confirm the predicted operation of the voltage controller. Regarding the generated power from the PV panels, it is possible to see from Figure 8b that, starting from zero, it will increase immediately until

it reaches the *MPP*. On the other hand, it is also possible to confirm that after reaching the *MPP*, it will stay at that point. In this way, the predicted capability of the proposed *MPPT* algorithm is confirmed.

Another transient test that was considered was the solar irradiance variation. Thus, initially a solar irradiance of 700 W/m^2 was considered, increasing to 1000 W/m^2 at 1.2 s and returning again to 800 W/m^2 at 1.8 s. This irradiance profile is shown in Figure 9a. The waveform of the *SRM* motor speed is shown in Figure 9b. As expected, with the increment in the *PV* generated power (due to the increase in the irradiance), there is also an increment in the motor speed, and vice versa. The behavior of the voltage controller is also presented through the *DC/DC* output voltages shown in Figure 9c. Indeed, this figure shows that these voltages remain in the reference value, confirming that the balance between the generated power and the power consumption of the motor is ensured.

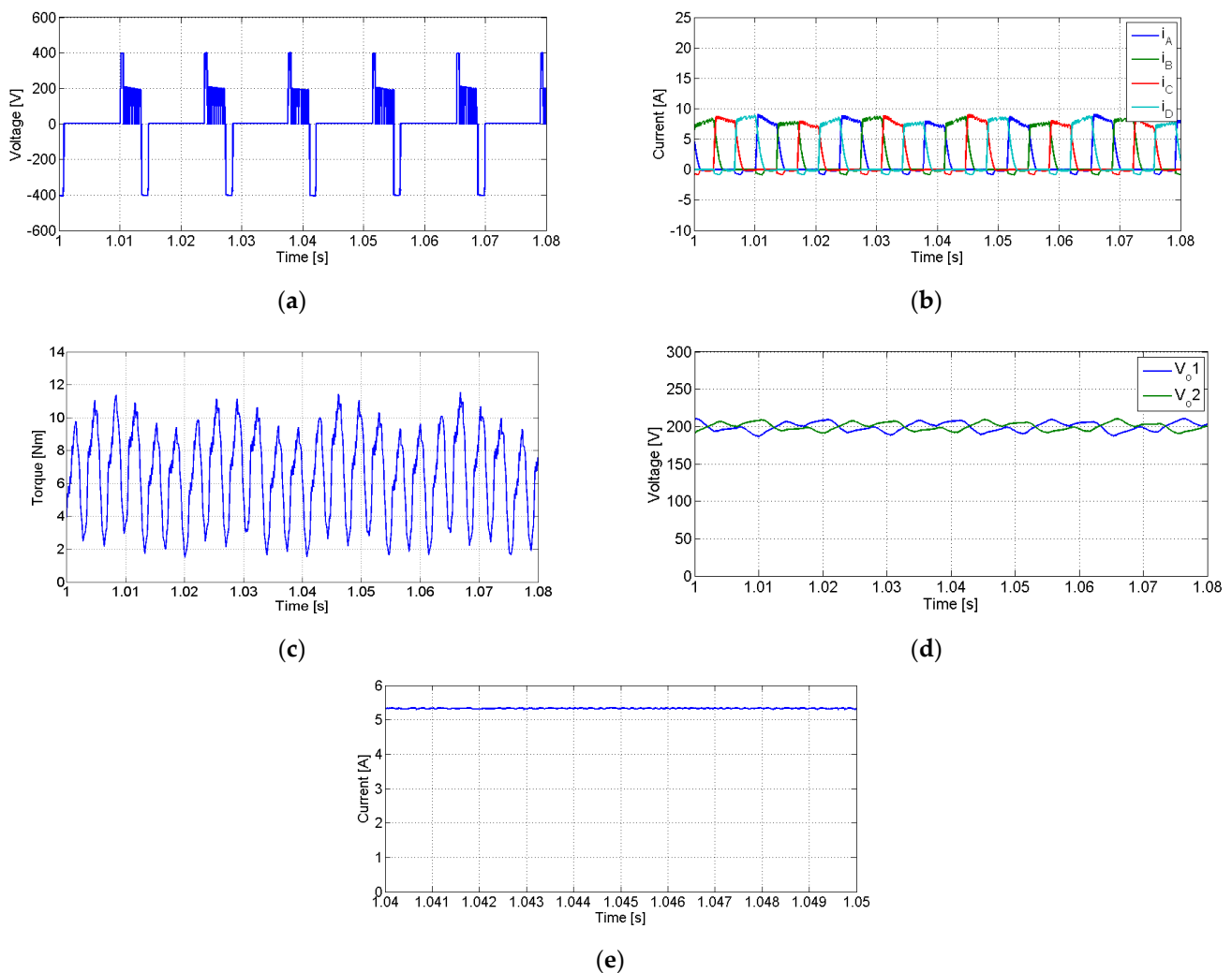


Figure 7. Obtained simulation waveforms for the tests in which an irradiance of 700 W/m^2 and an ambient temperature of $25 \text{ }^\circ\text{C}$ associated with the motor drive were defined: (a) motor winding *A* applied voltage, (b) currents in the motor windings, (c) *SRM* torque (d) input *DC* voltages applied to the drive, (e) converter input current.

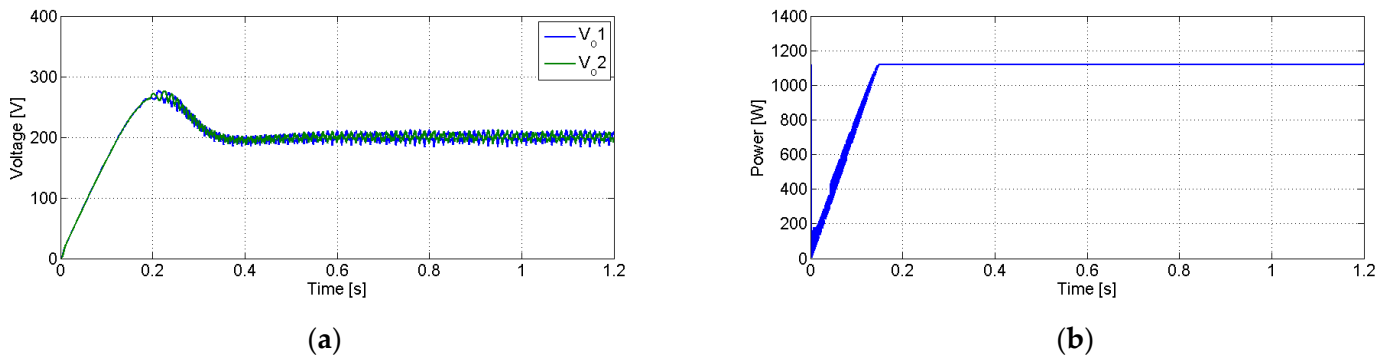


Figure 8. Obtained simulation waveforms during the connection of the system (transient operation): (a) DC/DC output voltages, (b) generated PV power.

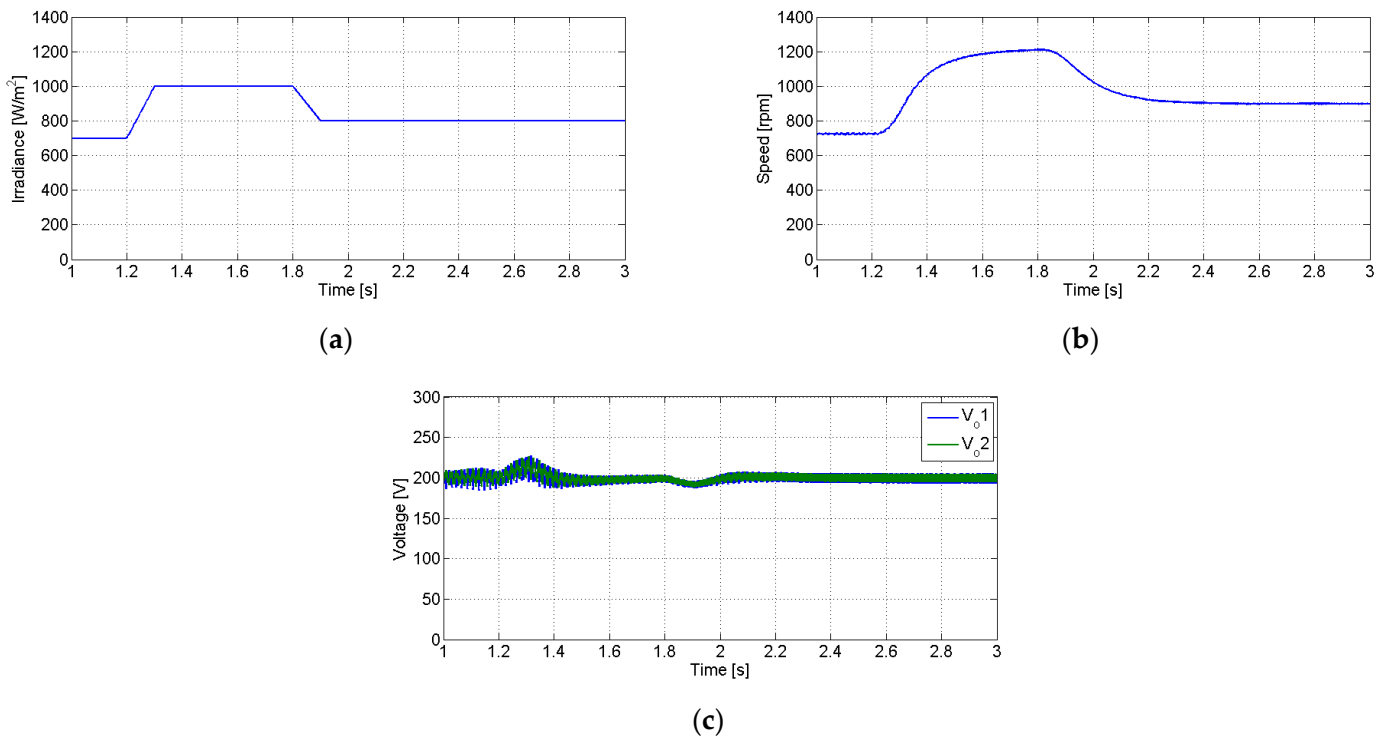


Figure 9. Obtained simulation waveforms during the connection of the system: (a) solar irradiation applied to the PV panels, (b) SRM motor speed, (c) DC/DC output voltages.

Tests with respect to various irradiances applied to the PV panel were also carried out. Thus, in order to see the impact of these changes in the system, in Figure 10, the obtained waveforms when the irradiance changes from 1000 W/m^2 to 400 W/m^2 in steps of 200 W/m^2 are presented. In Figure 10a, the irradiance applied to the PV panel is presented, and Figure 10b shows the motor speed. As expected, the motor speed changes with the irradiance once the generated power also changes. In fact, the motor speed changes from 1220 rpm to 170 rpm in steps just like the irradiance. It should be stated that in pumping systems, this change in speed is generally not very important, although it must be above a specific minimum value.

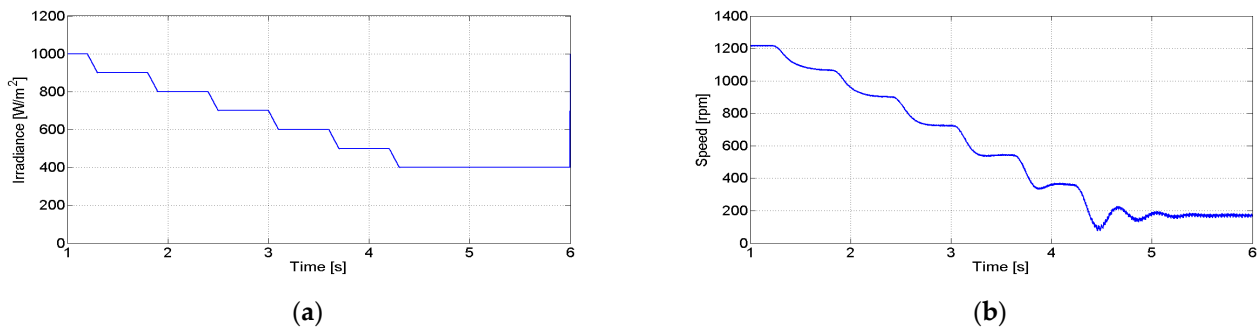


Figure 10. Obtained simulation waveforms with respect to various irradiances: (a) solar irradiation applied to the PV panels, (b) SRM motor speed.

5. Experimental Results

The proposed solution was also tested using a laboratory prototype combining the power electronic converters and the SRM. The parameters of the components used for this prototype were the same as the ones used for the simulation tests. The PV panels were simulated using a controlled voltage source (EA PS8360-30 2U) in which their characteristics were programmed to obtain the typical I–V curves. An 8/6 SRM machine was also used. Figure 11 shows the experimental test bench with the proposed laboratorial prototype. In figure, it is possible to see: 1—the controlled voltage source (EA PS8360-30 2U); 2—the digital signal processor (DSPACE 1104) used to control the multilevel SRM drive and MPPT algorithm; 3—the gate drive circuits; 4—the DC/DC converter; 5—the multilevel SRM drive; 6—the auxiliary power source for the gate drive circuits; 7—the signal generator; 8—the 8/6 SRM machine; 9—the absolute encoder for measuring speed and rotor position; 10—the DC machine used to simulate the water pump; 11—the current probes and 12—the DL1540 Yokogawa oscilloscope.

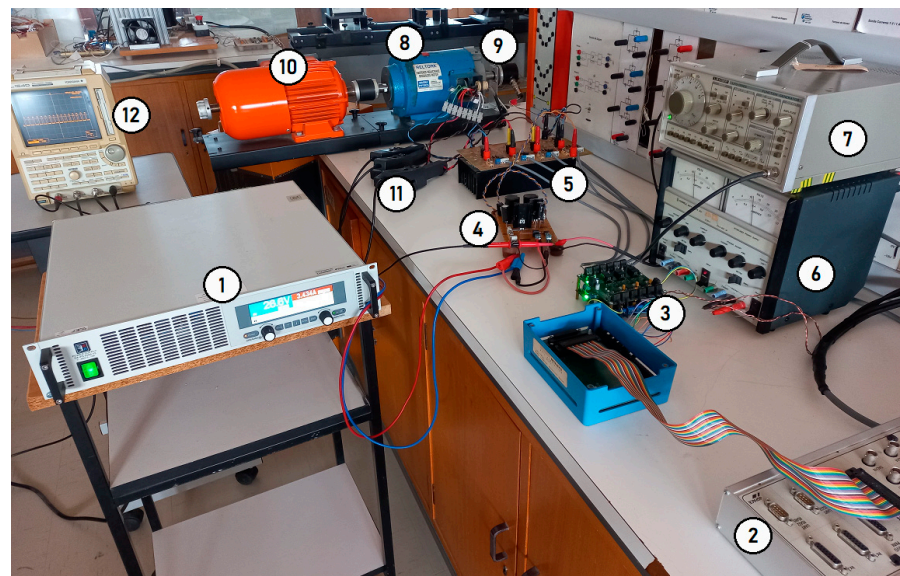


Figure 11. Photograph of the experimental test bench with the proposed laboratorial prototype: 1—controlled voltage source (EA PS8360-30 2U); 2—digital signal processor (DSPACE 1104) used to control the multilevel SRM drive; 3—gate drive circuits; 4—DC/DC converter; 5—multilevel SRM drive; 6—auxiliary power source for gate drive circuits; 7—signal generator; 8—8/6 SRM machine; 9—absolute encoder for measuring speed and rotor position; 10—DC machine used to simulate the water pump; 11—current probes; 12—DL1540 Yokogawa oscilloscope.

The laboratory results of the first test presented in Figure 12 were obtained in steady state considering a 700 W/m^2 irradiance and a $25 \text{ }^\circ\text{C}$ ambient temperature. The results shown in this figure are the voltage applied to motor winding A (Figure 12a) and currents in all the phases of the SRM (Figure 12b), as well as the output voltage (Figure 12c) and input current (Figure 12d) (applied to the SRM drive) of the DC/DC converter. From these waveforms, it is possible to conclude that they are similar to the ones obtained in the simulation tests. They also confirm the multilevel voltage characteristics of the SRM drive and continuous input current of the DC/DC converter.

Similar to the simulation tests, experimental transient tests were also performed. The first one was carried out considering the initial connection of the system. As shown in Figure 13, it is possible to conclude that the output voltage of the DC/DC converter starts at 0 V, but will rapidly achieve the desired (reference) value of 200 V. The balance of the DC/DC output capacitors voltages is also verified. It should be mentioned that, like in the simulation tests, the pumping system was only operated after the DC/DC output voltages reached the reference value.

A laboratory test in which the solar irradiance was not always constant was also performed. Thus, for this test, a first change in the solar irradiance from 700 W/m^2 to 1000 W/m^2 was implemented, then this irradiance was maintained and finally another change to 800 W/m^2 was implemented. The implemented solar irradiance, speed of the SRM and output voltages of the DC/DC converter results are presented in Figure 14. This figure confirms that the motor speed follows the irradiance and that the DC/DC output voltages are maintained at the reference value. These results also confirm the ones obtained in the simulation tests.

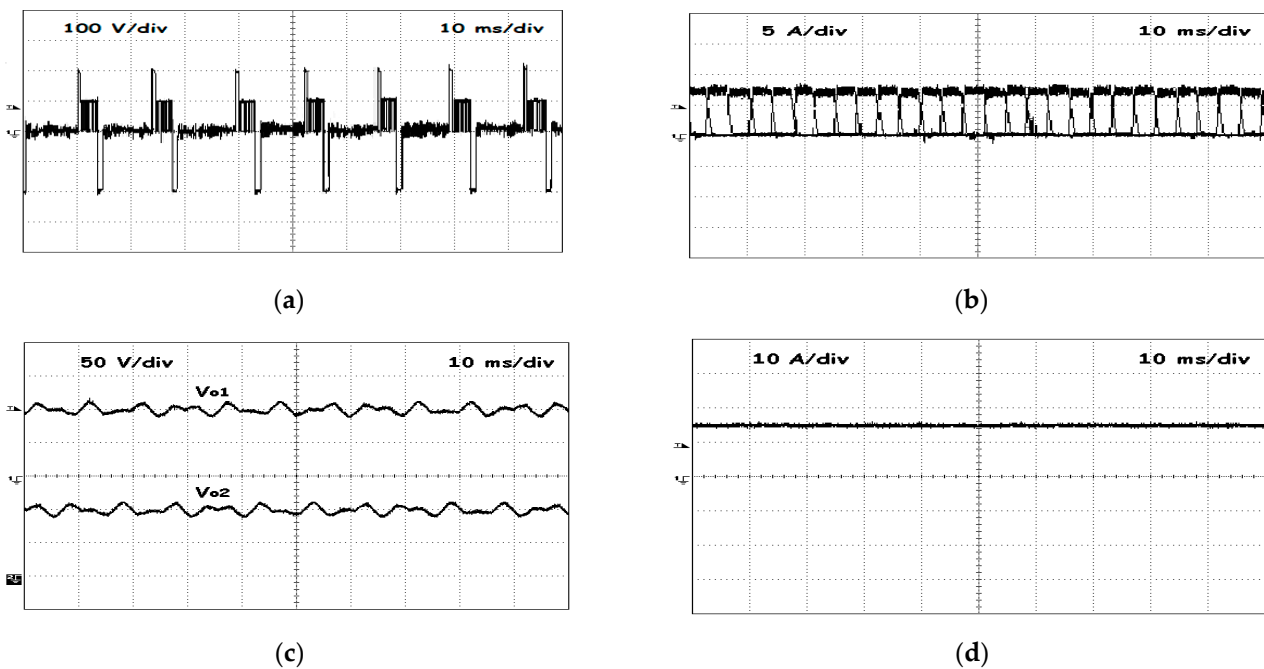


Figure 12. Obtained experimental waveforms for the tests in which 700 W/m^2 (irradiance) and $25 \text{ }^\circ\text{C}$ (ambient temperature) associated with the motor drive were defined: (a) voltage applied to motor winding A, (b) currents in all motor windings, (c) input DC voltages applied to the drive, (d) converter input current.

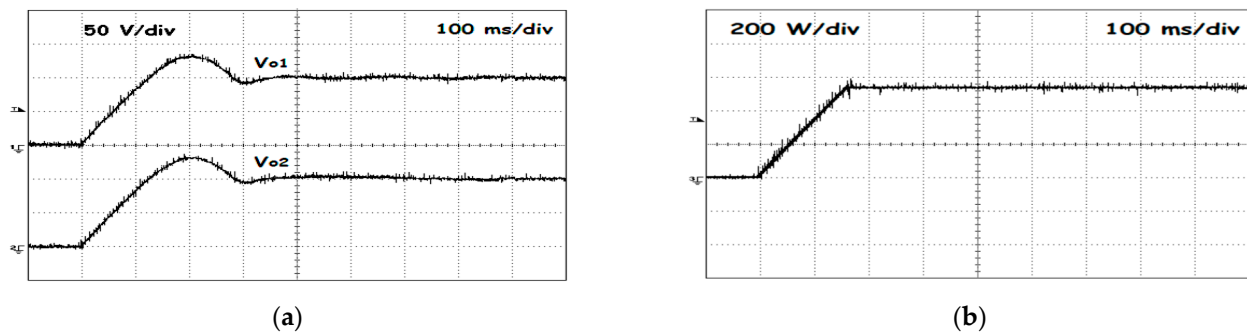


Figure 13. Obtained experimental waveforms for the tests in which 700 W/m^2 (irradiance) and $25 \text{ }^\circ\text{C}$ (ambient temperature) during the connection of the system were defined: (a) DC/DC output voltages, (b) generated PV power.

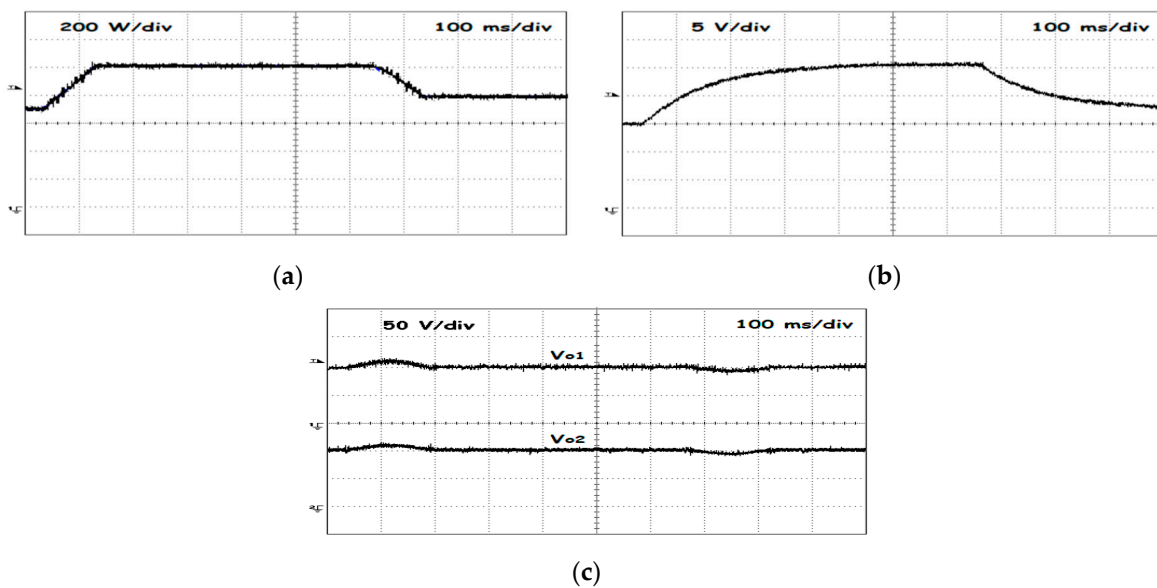


Figure 14. Obtained experimental waveforms when the system is subject to a change in the solar irradiance: (a) solar irradiation applied to the PV panels, (b) speed of the SRM motor ($22.5 \text{ V} \rightarrow 1000 \text{ rpm}$), (c) DC/DC output voltages.

6. Discussion

For a better analysis of the proposed system, a comparative study with other solutions is presented in this section. Since this system consists of two power electronic converters, the analysis will be focused on each of them. From the point of view of the SRM drive, several multilevel power converters have already been proposed. Table 2 presents the main characteristics associated with each one. As shown by this table, the asymmetric neutral point clamped (ANPC) [16] is the one that has more switches and diodes. This will lead to an increased cost of this drive. On the other hand, the cascaded asymmetric H-bridge [21] is the one that requires more than one independent voltage source. Thus, although requiring less diodes, this aspect will lead to an increase in the cost of this system. Among the classical multilevel structures, the T-Type [23] is considered one of the more interesting topologies. This structure requires the same number of switches, but uses a much lower number of extra diodes and does not require an extra independent voltage source. The adopted one allows for a clear reduction in the number of switches and diodes when compared with the other classical structures. Another point of view is regarding the DC converter associated with the PV panels and SRM drive. Another comparison is presented regarding other possible solutions. The main characteristics of each of these solutions can be seen in Table 3. From this table, it is possible to see that the one that was

adopted is among the ones that use fewer components. One of the topologies from this group that uses fewer passive components is the one from [41]. However, this topology only operates in boost mode, which can present some limitations for this kind of application. In fact, due to parasitic elements of inductors, capacitors and switching semiconductors, the voltage gain can strongly be limited, usually limited to around three times. Another interesting solution is the one from [43], although their input current is discontinuous, which, in this case, is not the best solution for PV panels.

Table 2. Comparison with typical multilevel power converters used in SRM drives.

Characteristics	Topology			
	[16]	[21]	[23]	Adopted
Number of switches	16	16	16	8
Extra diodes	32	14	8	8
Independent voltage sources	No	Yes	No	No
Cost	High	High	Medium	Low

Table 3. Comparison with DC/DC power converters used between the PV panels and the SRM drive.

Characteristics	Topology						
	[41]	[42]	[43]	[44]	[45]	[46]	Adopted
Voltage gain of each output	$\frac{1}{\delta}$	$\frac{1}{\delta}$	$\frac{1}{1-\delta}$	$\frac{1}{1-\delta}$	$\frac{1}{1-\delta}$	$\frac{1}{1-\delta}$	$\frac{1}{1-\delta}$
Number of switches	2	1	1	1	1	1	1
Number of diodes	3	3	2	2	4	3	2
Number of inductors	1	1	2	3	4	3	2
Number of capacitors	2	3	3	4	4	4	4
Input current	continuous	continuous	discontinuous	continuous	continuous	continuous	continuous

7. Conclusions

A water pumping system supplied by a PV generator and with a switched reluctance motor is presented in this paper. The purpose of this solution was to present a system with reduced costs. In this way, for the SRM drive, a multilevel converter with a reduced number of switches was adopted. Despite the reduced number of switches, the ability to magnetize and demagnetize the motor windings independently was maintained, as well as the provision of the DC voltage balance. For the DC/DC converter, associated with the PV panels and supplying energy to the motor drive, the same philosophy was adopted; it was designed with a single switch. The DC/DC converter is characterized by a dual output, which is a requirement for the SRM drive. On the other hand, the input current will be continuous, which is an important feature considering the use of PV. Associated with this converter, an MPPT algorithm was also implemented. The adoption of the proposed algorithm was selected due to easy implementation. In fact, it allows the use of a control law that is a function of the time derivative of the voltage and power, thus avoiding the singularities that can be found in this algorithm. Therefore, it is inclusively possible to implement this algorithm through a simple analogue circuit. The proposed system was verified through simulation and experimental tests using a laboratory prototype. These tests showed a good similarity, as well as the confirmation of the theoretical assumptions. From the theoretical assumption and performed tests, it was possible to verify that one conclusion that can be drawn from this work is that the speed of the motor is a function of the solar irradiance. This is due to the fact that by increasing solar irradiance, the generated power will also increase. In fact, tests in which the irradiance was changed from 1000 W/m² to 400 W/m² showed a change in the motor speed from 1220 rpm to 170 rpm.

Author Contributions: Conceptualization, V.F.P., H.C. and J.F.M.; methodology, V.F.P. and H.C.; simulations, V.F.P. and J.F.M.; validation, V.F.P., D.F., A.C., T.G.A. and A.P.; formal analysis, V.F.P. and J.F.M.;

investigation, V.F.P.; resources, V.F.P. and T.G.A.; data curation, V.F.P. and T.G.A.; writing—original draft preparation V.F.P., D.F. and A.C.; writing—review and editing, A.P. and A.C.; visualization, A.P. and A.C.; supervision, A.P.; project administration, J.F.M.; funding acquisition, A.P. and J.F.M. All authors have read and agreed to the published version of the manuscript.

Funding: This work was supported by national funds through the FCT—Fundação para a Ciência e a Tecnologia with reference UID/CEC/50021/2020 and UID/EEA/00066/2020.

Acknowledgments: This work was supported by national funds through the FCT—Fundação para a Ciência e a Tecnologia with reference UID/CEC/50021/2020 and UID/EEA/00066/2020.

Conflicts of Interest: The authors declare no conflict of interest.

References

1. Angadi, S.; Yaragatti, U.R.; Suresh, Y.; Raju, A.B. Comprehensive review on solar, wind and hybrid wind-PV water pumping systems—an electrical engineering perspective. *CPSS Trans. Power Electron. Appl.* **2021**, *6*, 1–19. [\[CrossRef\]](#)
2. Aliyu, M.; Hassan, G.; Said, S.A.; Siddiqui, M.U.; Alawami, A.T.; Elamin, I.M. A review of solar-powered water pumping systems. *Renew. Sustain. Energy Rev.* **2018**, *87*, 61–76. [\[CrossRef\]](#)
3. Bouzidi, B. Viability of solar or wind for water pumping systems in the Algerian Sahara regions—Case study Adrar. *Renew. Sustain. Energy Rev.* **2011**, *15*, 4436–4442. [\[CrossRef\]](#)
4. Liu, F.; Tait, S.; Schellart, A.; Mayfield, M.; Boxall, J. Reducing carbon emissions by integrating urban water systems and renewable energy sources at a community scale. *Renew. Sustain. Energy Rev.* **2020**, *123*, 1–14. [\[CrossRef\]](#)
5. Chilundo, R.J.; Neves, D.; Mahanjane, U.S. Photovoltaic water pumping systems for horticultural crops irrigation: Advancements and opportunities towards a green energy strategy for Mozambique. *Sustain. Energy Technol. Assess.* **2019**, *33*, 61–68. [\[CrossRef\]](#)
6. Kumar, S.S.; Bibin, C.; Akash, K.K.; Aravindan, K.; Kishore, M.; Magesh, G. Solar powered water pumping systems for irrigation: A comprehensive review on developments and prospects towards a green energy approach. *Mater. Today Proc.* **2020**, *33*, 303–307. [\[CrossRef\]](#)
7. Cloutier, M.; Rowley, P. The feasibility of renewable energy sources for pumping clean water in sub-Saharan Africa: A case study for Central Nigeria. *Renew. Energy* **2011**, *36*, 2220–2226. [\[CrossRef\]](#)
8. Mothilal Bhagavathy, S.; Pillai, G. PV Microgrid Design for Rural Electrification. *Designs* **2018**, *2*, 33. [\[CrossRef\]](#)
9. Kocan, S.; Rafajdus, P.; Bastovansky, R.; Lenhard, R.; Stano, M. Design and Optimization of a High-Speed Switched Reluctance Motor. *Energies* **2021**, *14*, 6733. [\[CrossRef\]](#)
10. Harris, M.R.; Miller, T.J.E. Comparison of design and performance parameters in switched reluctance and induction motors. In Proceedings of the Fourth International Conference on Electrical Machines and Drives Conference, London, UK, 13–15 September 1989; pp. 303–307.
11. Verma, S.; Mishra, S.; Chowdhury, S.; Gaur, A.; Mohapatra, S.; Soni, A.; Verma, P. Solar PV powered water pumping system—A review. *Mater. Today Proc.* **2021**, *46*, 5601–5606. [\[CrossRef\]](#)
12. Ramos, J.S.; Ramos, H.M. Solar powered pumps to supply water for rural or isolated zones: A case study. *Energy Sustain. Dev.* **2009**, *13*, 151–158. [\[CrossRef\]](#)
13. Ahn, J.; Lukman, G.F. Switched reluctance motor: Research trends and overview. *CES Trans. Electr. Mach. Syst.* **2018**, *2*, 339–347. [\[CrossRef\]](#)
14. Ellabban, O.; Abu-Rub, H. Switched reluctance motor converter topologies: A review. In Proceedings of the IEEE International Conference on Industrial Technology, Busan, Republic of Korea, 26 February 2014–1 March 2014; pp. 840–846.
15. Pires, V.F.; Pires, A.J.; Cordeiro, A.; Foito, D. A Review of the Power Converter Interfaces for Switched Reluctance Machines. *Energies* **2020**, *13*, 3490. [\[CrossRef\]](#)
16. Patil, D.; Wang, S.; Gu, L. Multilevel converter topologies for high-power high-speed switched reluctance motor: Performance comparison. In Proceedings of the IEEE Applied Power Electronics Conference and Exposition, Long Beach, CA, USA, 20–24 March 2016; pp. 2889–2896.
17. Deepak, M.; Janaki, G.; Bharatiraja, C. Power electronic converter topologies for switched reluctance motor towards torque ripple analysis. *Mater. Today Proc.* **2022**, *52*, 1657–1665. [\[CrossRef\]](#)
18. Peng, F.; Ye, J.; Emadi, A. An Asymmetric Three-Level Neutral Point Diode Clamped Converter for Switched Reluctance Motor Drives. *IEEE Trans. Power Electron.* **2017**, *32*, 8618–8631. [\[CrossRef\]](#)
19. Scholtz, P.A.; Gitau, M.N. Asymmetric Neutral Point Diode Clamped Topology with Reduced Component Count for Switched Reluctance Machine Drive. *Energies* **2022**, *15*, 2468. [\[CrossRef\]](#)
20. Yamada, N.; Hoshi, N. Experimental verification on a switched reluctance motor driven by asymmetric flying capacitor multilevel h-bridge inverter. In Proceedings of the IEEE 6th International Conference on Renewable Energy Research and Applications, San Diego, CA, USA, 5–8 November 2017; pp. 971–976.
21. Meng, R.; Wu, M. A Cascade Multilevel Converter of Switched Reluctance Motor and Its Control Timing Sequence. *Sens. Transducers* **2014**, *169*, 18–24.

22. Gengaraj, M.; Kalaivani, L.; Koodammal, K.; Krishnashini, M.; Aniana, L.; Prithi, S.D. A Comprehensive Study of Multilevel Inverter fed Switched Reluctance Motor for Torque Ripple Minimization with Multicarrier PWM Strategies. In Proceedings of the 4th International Conference on Electrical Energy Systems, Chennai, India, 7–9 February 2018; pp. 1–7.
23. Azer, P.; Bauman, J. An Asymmetric Three-Level T-Type Converter for Switched Reluctance Motor Drives in Hybrid Electric Vehicles. In Proceedings of the IEEE Transportation Electrification Conference and Expo, Detroit, MI, USA, 19–21 June 2019; pp. 1–6.
24. Lee, D.; Wang, H.; Ahn, J. An advanced multi-level converter for four-phase SRM drive. In Proceedings of the IEEE Power Electronics Specialists Conference, Rhodes, Greece, 15–19 June 2008; pp. 2050–2056.
25. Chowdhary, P.K.; Thakre, M.P. MMC based SRM Drives for Hybrid EV with Decentralized BESS. In Proceedings of the 4th International Conference on Electronics, Communication and Aerospace Technology, Coimbatore, India, 5–7 November 2020; pp. 319–325.
26. Gan, C.; Sun, Q.; Wu, J.; Kong, W.; Shi, C.; Hu, Y. MMC-Based SRM Drives with Decentralized Battery Energy Storage System for Hybrid Electric Vehicles. *IEEE Trans. Power Electron.* **2019**, *34*, 2608–2621. [[CrossRef](#)]
27. Gaafar, M.A.; Abdelmaksoud, A.; Orabi, M.; Chen, H.; Dardeer, M. Switched Reluctance Motor Converters for Electric Vehicles Applications: Comparative Review. *IEEE Trans. Transp. Electrification*. **2022**. [[CrossRef](#)]
28. Zan, X.; Xu, G.; Zhao, T.; Wang, R.; Dai, L. Multi-Battery Block Module Power Converter for Electric Vehicle Driven by Switched Reluctance Motors. *IEEE Access* **2021**, *9*, 140609–140618. [[CrossRef](#)]
29. Pires, V.F.; Foito, D.; Pires, A.J.; Cordeiro, A.; Martins, J.F. An 8/6 SRM Drive with a Multilevel Converter Based on an NPC Structure and Designed to Provide Transistor Fault Tolerant Capability. In Proceedings of the 16th IEEE International Conference on Compatibility, Power Electronics and Power Engineering, Birmingham, UK, 29 June 2022–1 July 2022; pp. 1–6.
30. Zan, X.; Wu, N.; Xu, R.; Cui, M.; Jiang, Z.; Ni, K.; Alkahtani, M. Design and Analysis of a Novel Converter Topology for Photovoltaic Pumps Based on Switched Reluctance Motor. *Energies* **2019**, *12*, 2526. [[CrossRef](#)]
31. Mishra, A.K.; Singh, B.; Kim, T. An Efficient and Credible Grid-Interfaced Solar PV Water Pumping System with Energy Storage. *IEEE J. Photovolt.* **2022**, *12*, 880–887. [[CrossRef](#)]
32. Chaurasiya, S.K.; Bhattacharya, A.; Das, S. Reduced switch multilevel converter topology to improve magnetization and demagnetization characteristics of an SRM. In Proceedings of the IEEE International Conference on Power Electronics, Smart Grid, and Renewable Energy, Trivandrum, India, 2–5 January 2022; pp. 1–6.
33. Rao, M.N.; Karthick, N.; Rao, A.M. Fault Tolerant Ability of A Multi Level Inverter Fed Three Phase Induction Motor for Water Pumping Application. In Proceedings of the 7th International Conference on Electrical Energy Systems, Chennai, India, 11–13 February 2021; pp. 212–216.
34. Koreboina, V.B.; Narasimharaju, B.L.; Kumar, D.M.V. Performance investigation of simplified PWM MPPT approach for direct PV-fed switched reluctance motor in water pumping system. *IET Electr. Power Appl.* **2017**, *11*, 1645–1655. [[CrossRef](#)]
35. Wang, X.; Gan, C.; Hu, Y.; Cao, W.; Chen, X. Renewable energy-fed switched reluctance motor for PV pump applications. In Proceedings of the 2014 IEEE Conference and Expo Transportation Electrification Asia-Pacific, Beijing, China, 31 August 2014–3 September 2014; pp. 1–6.
36. Oshaba, A.S.; Ali, E.S.; Elazim, S. PI controller design for MPPT of photovoltaic system supplying SRM via BAT search algorithm. *Neural Comput. Appl.* **2017**, *28*, 651–667. [[CrossRef](#)]
37. Oshaba, A.S.; Ali, E.S.; Abd Elazim, S.M. MPPT control design of PV system supplied SRM using BAT search algorithm. *Sustain. Energy Grids Netw.* **2015**, *2*, 51–60. [[CrossRef](#)]
38. Oliver, J.S.; David, P.W.; Balachandran, P.K.; Mihet-Popa, L. Analysis of Grid-Interactive PV-Fed BLDC Pump Using Optimized MPPT in DC–DC Converters. *Sustainability* **2022**, *14*, 7205. [[CrossRef](#)]
39. Yalavarthi, A.; Singh, B. Sensorless SRM driven Solar Irrigation Pump with Grid-Support Using Vienna Rectifier. In Proceedings of the 3rd International Conference on Energy, Power and Environment: Towards Clean Energy Technologies, Shillong, Meghalaya, India, 5–7 March 2021; pp. 1–6.
40. Cordeiro, A.; Pires, V.F.; Foito, D.; Pires, A.J.; Martins, J.F. Three-level quadratic boost DC-DC converter associated to a SRM drive for water pumping photovoltaic powered systems. *Sol. Energy* **2020**, *209*, 42–56. [[CrossRef](#)]
41. Mishra, A.K.; Singh, B. An Improved Control Technique for Grid Interactive 4-Phase SRM Driven Solar Powered WPS Using Three-Level Boost Converter. *IEEE Trans. Ind. Inform.* **2021**, *17*, 290–299. [[CrossRef](#)]
42. Sulake, N.R.; Devarasetty Venkata, A.K.; Choppavarapu, S.B. FPGA Implementation of a Three-Level Boost Converter-fed Seven-Level DC-Link Cascade H-Bridge inverter for Photovoltaic Applications. *Electronics* **2018**, *7*, 282. [[CrossRef](#)]
43. Mishra, A.K.; Singh, B. Solar Photovoltaic Array Dependent Dual Output Converter Based Water Pumping Using Switched Reluctance Motor Drive. *IEEE Trans. Ind. Appl.* **2017**, *53*, 5615–5623. [[CrossRef](#)]
44. Mishra, A.K.; Singh, B. Design of solar-powered agriculture pump using new configuration of dual-output buck–boost converter. *IET Renew. Power Gener.* **2018**, *12*, 1640–1650. [[CrossRef](#)]
45. Luo, F.L. Double-output Luo converters, an advanced voltage-lift technique. *IEE Proc. -Electr. Power Appl.* **2000**, *147*, 469–485. [[CrossRef](#)]
46. Marjani, J.; Imani, A.; Hekmati, A.; Afjei, E. A new dual output DC-DC converter based on SEPIC and Cuk converters. In Proceedings of the 2016 International Symposium on Power Electronics, Electrical Drives, Automation and Motion (SPEEDAM), Capri, Italy, 22–24 June 2016; pp. 946–950.

47. Joseph, A.; Kim, S.M.; Lee, S.; Dominic, A.; Lee, K.B. Boost multi-level NPC-fed VS large rated asynchronous pumped storage hydro-generating unit. *IET Electr. Power Appl.* **2019**, *13*, 1488–1496. [[CrossRef](#)]
48. Rahman, S.; Meraj, M.; Iqbal, A.; Tariq, M.; Maswood, A.; Ben-Brahim, L.; Al-Ammari, R. Design and Implementation of Cascaded Multilevel qZSI Powered Single-Phase Induction Motor for Isolated Grid Water Pump Application. *IEEE Trans. Ind. Appl.* **2020**, *56*, 1907–1917. [[CrossRef](#)]
49. Pires, V.F.; Foito, D.; Cordeiro, A.; Chaves, M.; Pires, A.J. PV Generator-Fed Water Pumping System Based on a SRM with a Multilevel Fault-Tolerant Converter. *Energies* **2022**, *15*, 1–19. [[CrossRef](#)]
50. Haq, S.; Biswas, S.P.; Kamal Hosain, M.; Islam, M.R.; Ashib Rahman, M.; Muttaqi, K.M. A Modified PWM Scheme to Improve the Power Quality of NPC Inverter Based Solar PV Fed Induction Motor Drive for Water Pumping. In Proceedings of the IEEE Industry Applications Society Annual Meeting, IAS 2021, Vancouver, BC, Canada, 10–14 October 2021; pp. 1–6.
51. Bollipo, R.B.; Mikkili, S.; Bonthagorla, P.K. Hybrid, optimal, intelligent and classical PV MPPT techniques: A review. *CSEE J. Power Energy Syst.* **2021**, *7*, 9–33.
52. Pathy, S.; Subramani, C.; Sridhar, R.; Thentral, T.M.T.; Padmanaban, S. Nature-Inspired MPPT Algorithms for Partially Shaded PV Systems: A Comparative Study. *Energies* **2019**, *12*, 1451. [[CrossRef](#)]
53. Radhakrishnan, R.K.G.; Marimuthu, U.; Balachandran, P.K.; Shukry, A.M.M.; Senjyu, T. An Intensified Marine Predator Algorithm (MPA) for Designing a Solar-Powered BLDC Motor Used in EV Systems. *Sustainability* **2022**, *14*, 14120. [[CrossRef](#)]
54. Pires, V.F.; Foito, D.; Pires, A.J.; Cordeiro, A.; Martins, J.F.; Chen, H. Multilevel Converter Fed SRM Drive for Single Stage PV Array Based Water Pumping. In Proceedings of the 45th Annual Conference of the IEEE Industrial Electronics Society (IECON 2019), Lisbon, Portugal, 14–17 October 2019; pp. 6495–6500.
55. Markkassery, S.; Saradagi, A.; Mahindrakar, A.D.; Lakshminarasamma, N.; Pasumarthy, R. Modeling, Design and Control of Non-isolated Single-Input Multi-Output Zeta–Buck–Boost Converter. *IEEE Trans. Ind. Appl.* **2020**, *56*, 3904–3918.
56. Pina, M.; Pires, V.F. Grid-Connected PV System Using a T-Type qZS Inverter with an Integral Time Derivative Approach to Ensure MPP and Decoupled Current Control. In Proceedings of the 2020 International Young Engineers Forum, Costa da Caparica, Portugal, 3 July 2020; pp. 38–43.

Disclaimer/Publisher’s Note: The statements, opinions and data contained in all publications are solely those of the individual author(s) and contributor(s) and not of MDPI and/or the editor(s). MDPI and/or the editor(s) disclaim responsibility for any injury to people or property resulting from any ideas, methods, instructions or products referred to in the content.